IOP Publishing Journal of Physics: Condensed Matter
J. Phys.: Condens. Matter **34** (2022) 105702 (13pp) https://doi.org/10.1088/1361-648X/ac431d

Topological phase and thermoelectric properties of bialkali bismuthide compounds $(Na, K)_2RbBi$ from first-principles

Shahram Yalameha[1], Zahra Nourbakhsh[1,*] and Daryoosh Vashaee[2,3,*]

[1] Faculty of Physics, University of Isfahan, 81746-73441, Isfahan, Iran
[2] Department of Electrical and Computer Engineering, North Carolina State University, Raleigh, NC 27606, United States of America
[3] Department of Materials Science and Engineering, North Carolina State University, Raleigh, NC 27606, United States of America

E-mail: z.nourbakhsh@sci.ui.ac.ir and dvashae@ncsu.edu

Received 18 September 2021, revised 29 November 2021
Accepted for publication 14 December 2021
Published 28 December 2021

Abstract

We report the topological phase and thermoelectric properties of bialkali bismuthide compounds $(Na, K)_2RbBi$, as yet hypothetical. The topological phase transitions of these compounds under hydrostatic pressure are investigated. The calculated topological surface states and Z_2 topological index confirm the nontrivial topological phase. The electronic properties and transport coefficients are obtained using the density functional theory combined with the Boltzmann transport equation. The relaxation times are determined using the deformation potential theory to calculate the electronic thermal and electrical conductivity. The calculated mode Grüneisen parameters are substantial, indicating strong anharmonic acoustic phonons scattering, which results in an exceptionally low lattice thermal conductivity. These compounds also have a favorable power factor leading to a relatively flat p-type figure-of-merit over a broad temperature range. Furthermore, the mechanical properties and phonon band dispersions show that these structures are mechanically and dynamically stable. Therefore, they offer excellent candidates for practical applications over a wide range of temperatures.

Keywords: topological materials, thermoelectric, thermal conductivity, bialkali bismuthide

Supplementary material for this article is available online

(Some figures may appear in colour only in the online journal)

1. Introduction

Energy crisis and environmental pollution, two critical challenges of the current century, are primarily due to high dependence on fossil fuels. Addressing these problems has motivated many researchers to develop energy conversion technologies that are green and eco-friendly. With nearly two-thirds of the world's energy wasted as heat, thermoelectric (TE) materials offer a practical approach to recycle some part of it and contribute significantly to energy saving. The energy conversion efficiency of TE materials is often determined using the dimensionless figure of merit (zT) given by $zT = S^2\sigma T/\kappa$, where S, σ, T and κ are the Seebeck coefficient (thermopower), electrical conductivity, absolute temperature,

* Authors to whom any correspondence should be addressed.

and thermal conductivity. Thermal conductivity κ has contributions from the electronic κ_e and lattice κ_l thermal conductivity, i.e., $\kappa = \kappa_e + \kappa_l$. Also, the power factor (PF) is defined as $PF = S^2\sigma$. High-efficiency TE materials usually require a large Seebeck coefficient or high PF, high electrical conductivity, and low thermal conductivity. These parameters are usually counter-indicative and change with the carrier concentration [1, 2]. For example, the large Seebeck coefficient usually happens at low carrier concentration, leading to low electrical conductivity. Also, increasing the electrical conductivity usually increases the thermal conductivity [3]. The interdependency of these parameters explains why achieving a high zT is challenging. As such, new ideas have been developed over the last two decades and based on these ideas, new materials and structures have been designed and synthesized. Some approaches focused on improving the PF, such as carrier pocket engineering [4–6], complex structures [7, 8], carrier energy filtering [9, 10], creation of resonant energy levels close to the band edges [11], and low dimensional structures [12, 13]. Another approach to enhance the zT is to reduce the lattice thermal conductivity. Some examples in this direction are methods to enhance phonon scattering via nano inclusions [14–16], nanostructuring [17, 18], or using materials with large unit cells such as clathrates [3] and skutterudites [19].

Additionally, TE materials in nano bulk forms such as nanostructured single component bulk structures and multicomponent nanocomposites have been investigated extensively due to their relatively inexpensive and simple synthesis and compatibility with the commercial TE devices [20, 21]. However, it is worth mentioning that although the nanostructuring concept improved the zT of many material systems-[22, 23], the excessive interfaces deteriorated the carrier mobility in some materials so strongly that nanostructuring led to little or no improvement in zT and, in some cases, even reduced the zT [24–26].

Topological insulators (TIs) represent a new quantum state of matter characterized by a peculiar and unique edge or surface state [27]. These topological materials may also offer a new direction for making high-performance TE materials [1, 28–32]. In TIs, the spins of Dirac fermions are tightly locked with their momentum so that the charge carriers on the boundary states of these materials experience no backscattering at impurities and defects, which is beneficial for low-dispassion transport. Furthermore, the zT of these materials can be improved by optimizing the geometry size for the contributions of the boundary and bulk states [3, 31]. In addition to TIs, Weyl/Dirac semimetals form another class of topological materials with unique properties [27, 33]. Interestingly, similar to the surface states of TIs, topological surface states (TSS) also exist on the surface of these materials called Fermi arcs [33]. In addition to these surface states, chiral magnetic effects and negative magnetoresistance have been observed in the bulk of these materials [27]. Apart from some basic features that connect both TE and topological materials, such as heavy elements and small band gaps, the observation of some TE phenomena has led to more attention on these materials [3, 31]. Recent studies have shown that the transverse thermoelectricity of topological semimetals is promising for solid-state cooling applications [34, 35]. For example, by investigating the Nernst effect in the Dirac semimetal Cd_3As_2, a transverse zT can be defined for this compound that amounts to 0.5 at 2 T at room temperature [36]. Furthermore, a large, nonsaturating Seebeck effect in quantizing magnetic fields has been obtained for topological Dirac/Weyl semimetals [37]. Interestingly, it has been found that such a transverse TE effect (i.e., transverse zT) is easily optimized by adjusting the Fermi level toward the Dirac/Weyl nodes. Also, topological semimetals can have an additional transverse TE effect, known as the anomalous Nernst effect, which results from the Berry curvature near the Fermi level [38].

Consequently, topological materials, along with many other purposes, have taken much attention for TE applications. So far, broad varieties of TE materials have been investigated for various temperature regimes. Compounds containing alkali metals with antimony and bismuth yield a group of exciting semiconductors. In recent years, bismuthides and bialkali antimonides structures have had various functional applications in photodetectors and emitters materials, TE energy conversion, linear optical properties, sensing devices, and even topological phases [39–47]. However, to date, mostly alkali antimonide compounds have been studied theoretically primarily. In contrast, no comprehensive study has been devoted to examining the structural, elastic, topological phase, and TE properties of bialkali bismuthide compounds $(Na, K)_2RbBi$ regardless of their prospective technological applications.

In the present study, the first-principles calculations are applied to estimate the TE performance and topological phase evolution of bialkali bismuthides compounds $(Na, K)_2RbBi$ under hydrostatic pressures. The electronic transport properties of these compounds are investigated by calculating the electronic band structures and solving Boltzmann transport equations. Furthermore, the electronic relaxation time is obtained using the deformation potential theory (DPT).

The maximum figure of merit zT of p-type Na_2RbBi (K_2RbBi) compound can reach 0.80 (0.87) at 300 K (1000 K). Therefore, it is predicted that Na_2RbBi (K_2RbBi) compound should be a promising room (high) temperature TE material. Our calculations of the mechanical properties and phonon band dispersions show that these structures are mechanically and dynamically stable. The topological phase transition (TPT) point, within TB-mBJ and PBE-GGA approaches, has also been evaluated under hydrostatic pressures. Hence, band inversion, Z_2 topological index, and TSS are investigated.

2. Computational details

All calculations are performed using the full-potential linearized augmented plane wave [48] method based on density functional theory using the WIEN2K package [49]. For the structural optimization and electronic properties, we used the exchange–correlation potential within the PBE-GGA approach [50]. More precisely, to calculate the electronic band structure, specifically the bandgaps, we used an enhanced version of Becke–Johnson (mBJ) potential, suggested by Tran and Blaha [51]. The 17 × 17 × 17 Monkhorst–Pack $\boldsymbol{k}$-mesh

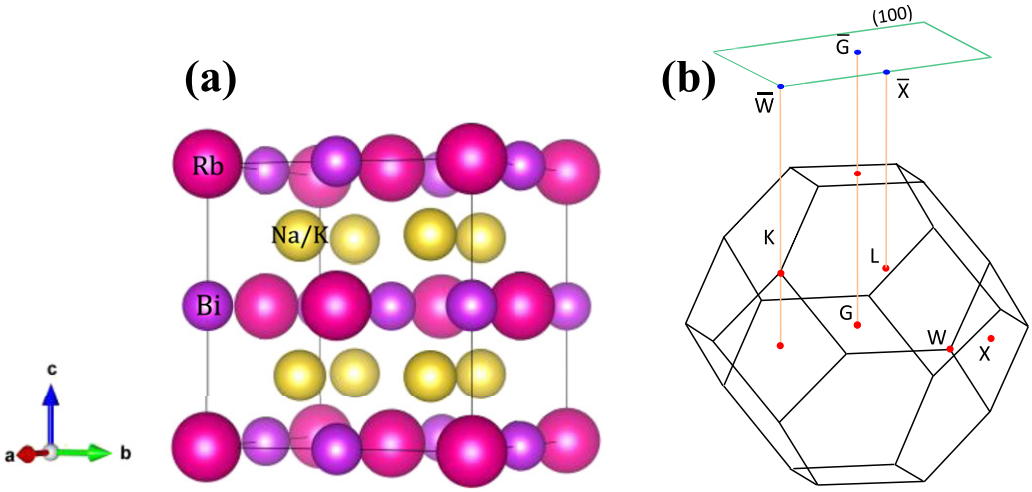

Figure 1. (a) The crystal structure of (Na, K)$_2$RbBi within *Fm*-3*m* (No. 225) space group, where the structural co-ordinates of Na/K are 8 (C) (1/4, 1/4, 1/4), Rb are 4(a) (0, 0,0) and Bi are 4(b) (1/2, 1/2, 1/2), respectively. (b) The first 3D/2D BZ and the high-symmetry points.

sampling in the Brillouin zone (BZ) is used for the geometrical optimization and self-consistent calculations, while a large $\boldsymbol{k}$-mesh of 47 × 47 × 47 is used to obtain an adequately accurate band structure for the calculations of transport coefficients. The spin–orbit coupling is considered in the calculations of the electronic, TE, and mechanical properties. The Phonopy code [52] is used for phonon dispersion and Grüneisen parameter calculations. The TE transport properties and coefficients are calculated from the electronic structure using semiclassical Boltzmann theory, implemented in the BoltzTraP package [53]. The lattice thermal conductivity was obtained by the modified Debye–Callaway model [54]. The elastic properties were calculated using IRELAST [55] and ELATOOLS [56] packages.

We used the DPT for the relaxation time to evaluate the electronic transport performance. Based on this theory, one can calculate the relaxation time (τ) along the *i*-direction [57, 58] by:

$$\tau = \frac{2\sqrt{2\pi}C_i\hbar^4}{3(k_BTm^*_{dos})^{3/2}E_i^2}, \tag{1}$$

where C_i is the elastic constant, E_i is the DP constant, and $m^*{}_{dos}$ is the density-of-state (DOS) effective mass (calculated using perturbation approach in MSTAR code [59]). C_i is the elastic constant from $C_{11}(=C_{22}=C_{33})$, which is calculated using the IRelast package. The DP constant E_i is calculated by

$$E_i = \frac{\partial E_{edge}}{\partial(\Delta l)/l_0}, \tag{2}$$

where E_{edge} is the energy of the valence or conduction band edge in relation to the lattice deformation quantity along the *i*-direction of external strain [57, 60], and l_0 is the equilibrium lattice constant. By applying strains of -6×10^{-4}, -3×10^{-4}, 0.00, $+3 \times 10^{-4}$, and $+6 \times 10^{-4}$ percentage of $\Delta l/l_0$, we obtain E_i by fitting the curve of E_{edge} according to equation (2). The details are collected in figures S1 and S2 of supporting information file (https://stacks.iop.org/JPCM/34/105702/mmedia). The TSS and Wannier charge centers (WCCs) are obtained by constructing the maximally localized Wannier functions (WANNIER90 code [61]) and using the iterative Green function method [62] and Wilson-loop method [63, 64], respectively. The Wilson-loop for the insulator systems is defined in terms of the projector ($P^{occ}_{\mathbf{k}}$) onto the N_{occ} occupied (occ) states, $u_{j\boldsymbol{k}}$, as [65, 66],

$$P^{occ}_{\mathbf{k}} = \sum_{j=1}^{N_{occ}} |u_{j\mathbf{k}}\rangle \langle u_{j\mathbf{k}}|, \qquad W_{loop}(C) = \prod_{i=0}^{L-1} P^{occ}_{\mathbf{k}_i}, \tag{3}$$

where C is a closed curve in $\boldsymbol{k}$-space, discretized in L points k_i, $i = 0,\ldots, L-1$, and the $W_{loop}(C)$ is a $N_{occ} \times N_{occ}$ matrix. Based on this, by taking the log of the eigenvalues of the $W_{loop}(C)$ at an arbitrary point on the loop C and normalizing by 2π, we arrive at a special gauge-invariant set of hybrid WCCs, which exactly coincide with those obtained from the maximally localized WCC (more details can be found in references [66–69]).

3. Results and discussion

3.1. Structural, phonon, and mechanical properties

Bialkali bismuthides compounds of (Na, K)$_2$RbBi kind crystallize in fcc structure within *Fm*-3*m* (No. 225) space group, where the structural coordinates of Na/K are 8(c) (1/4, 1/4, 1/4), Rb are 4(a) (0.0, 0.0, 0.0) and Bi are 4(b) (1/2, 1/2, 1/2), respectively (see figure 1(a)). The calculated lattice constants of Na$_2$RbBi and K$_2$RbBi are 8.17 and 8.90 Å.

The dynamical stability is the crucial criterion for a material to be synthesized practically [70]. These criteria for (Na, K)$_2$RbBi compounds can be predicted from the phonon dispersion curves. The calculated phonon dispersion curves along with the high-symmetry points (see figure 1(b)) and the partial phonon density of states (PDOSs) are shown in figure 2.

The positive phonon frequency of these compounds over the whole BZ indicates that these compounds are thermodynamically stable and can be potentially synthesized in the laboratory. According to the phonon dispersion curves, three

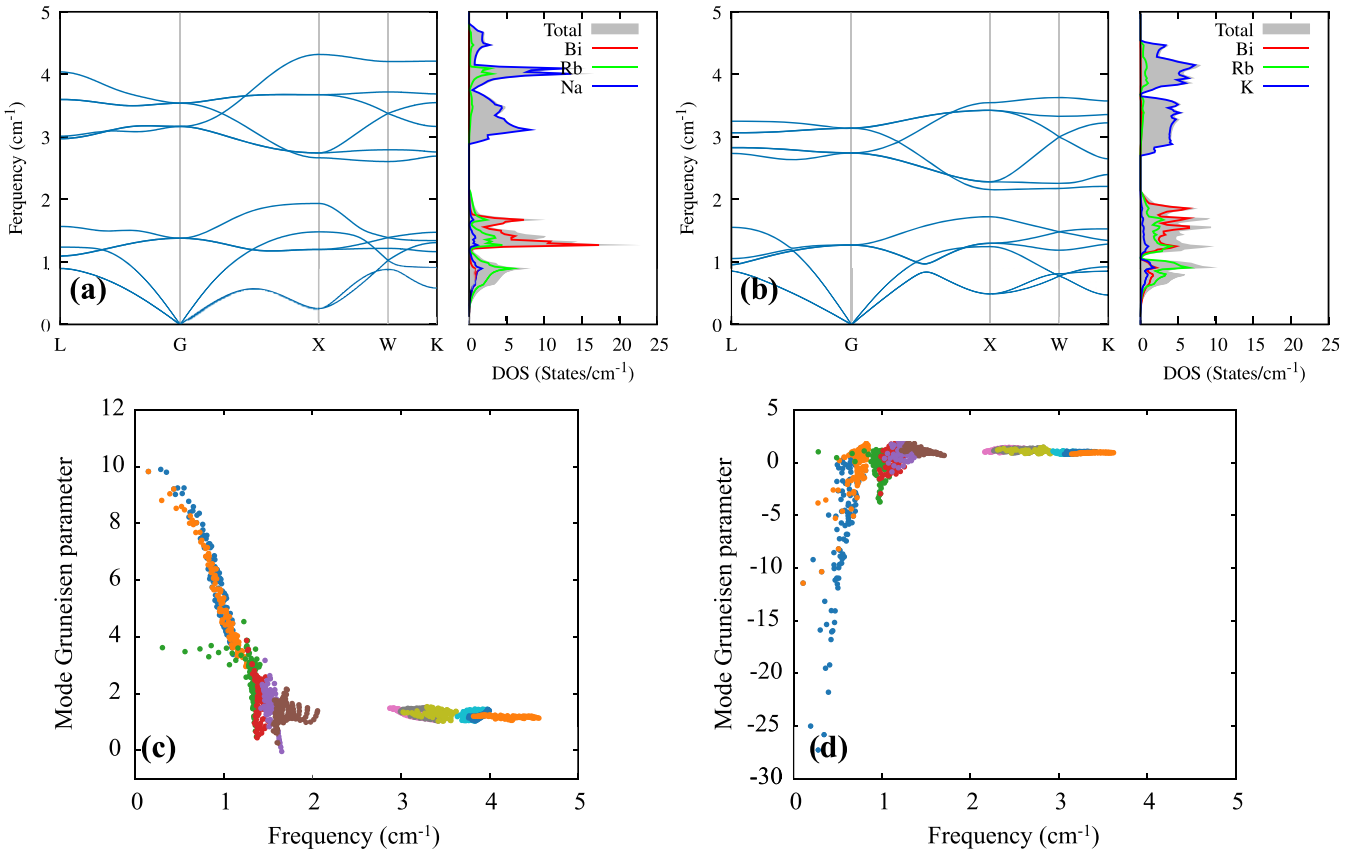

Figure 2. Phonon dispersion relations and partial PDOSs of (a) Na_2RbBi and (b) K_2RbBi along with high-symmetry points. From PDOS, it can be seen that Bi, Rb, and K/Na induce three acoustic phonons, where Rb has dominant contributions. There is no gap between acoustic and optical phonon modes, which is non-conducive for heat conduction by phonons, indicating relatively moderate phonon scattering in these compounds. Computed phonon mode of Grüneisen parameter of (c) Na_2RbBi and (d) K_2RbBi. The mode Grüneisen parameter for each mode are shown by different colors. The acoustic phonons have huge Grüneisen parameters suggesting the existence of strong anharmonic scattering between acoustic phonons.

acoustic and nine optical phonon branches are observed due to four atoms per unit cell. From PDOS, we see that Bi, Rb, and K/Na induce three acoustic phonons, with Rb having the dominant contributions. The lack of energy gap between the optical and acoustic phonon modes indicates a moderate phonon scattering in these compounds. The first four optical modes of frequency $\sim$1–1.8 cm^{-1} arise from Rb and Bi, with a small contribution of K/Na. Six higher energy optical phonon modes come from Na/K, suggesting that Na/K has a negligible contribution in the lattice thermal conductivity. A larger Grüneisen parameter indicates a more anharmonic behavior of the system. Therefore, the Grüneisen parameters inversely affect the lattice thermal conductivity. Figures 2(c) and (d) illustrate the mode Grüneisen parameters. It can be seen that the acoustic phonons have large Grüneisen parameters evidencing a strong anharmonic scattering among acoustic phonons.

Elastic constants (C_{ij}) have been calculated to investigate the mechanical stability conditions and to calculate the relaxation time (τ). The calculated elastic constants C_{ij} and other elastic parameters of these compounds are given in table S1. These compounds strictly followed the mechanical stability conditions derived by Born *et al* [70–72]. Interestingly, the calculation results on the spatial dependence of the Poisson's ratio show that K_2RbBi has a negative Poisson's ratio (NPR) and Na_2RbBi has a positive Poisson's ratio. The spatial dependence (2D heat maps) and 2D projection in the *xy*-plane of Poisson's ratio are illustrated in (figure S3) figure S4. Figure S4(b) shows that K_2RbBi has a significant NPR in the [110], [101], and [011] directions, making this compound a 3D *auxetic* material.

3.2. Electronic structure and TPT

The calculation of the electronic band structure is essential to understand the electronic properties of materials, which almost completely explain the band inversion for the topological phase and transport properties. The PBE-GGA approach usually underestimates the experimental bandgaps [71]; however, the TB-mBJ approach can predict bandgaps comparable with experimental values [72]. Therefore, in this work, we have obtained the electronic band structures using two different exchange–correlation approaches PBE-GGA and TB-mBJ. The electronic band structures of (Na, K)$_2$RbBi along with high-symmetry points (see figure 1(b)) within the PBE-GGA and TB-mBJ approaches are displayed in figure S5. As shown in figures S5(a) and (b), these compounds are zero-gap semimetals within PBE-GGA approach, while in the

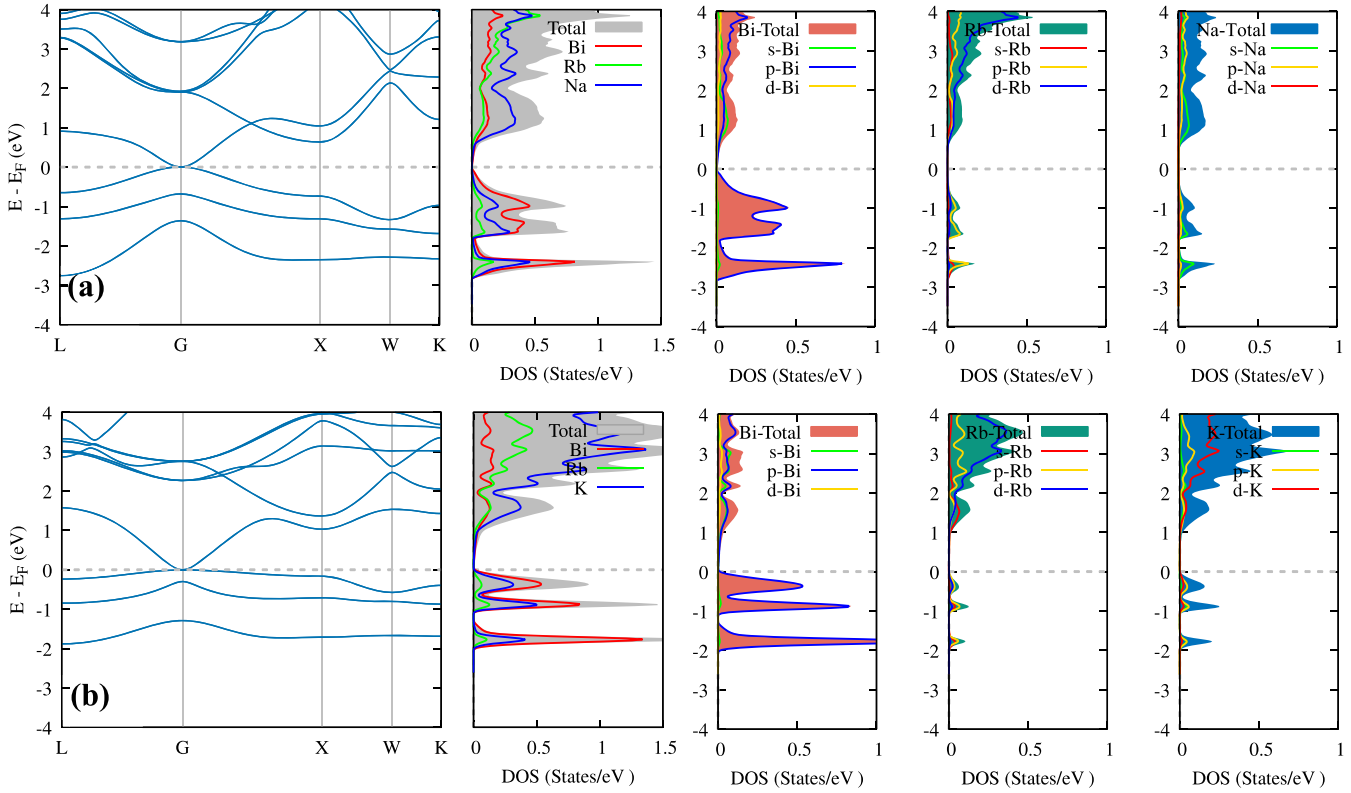

Figure 3. Calculated TDOSs and PDOS (a) Na_2RbBi and (b) K_2RbBi computed using PBE-GGA functional. The Fermi energy is set to zero. The valence band in PDOS near the Fermi level is mainly attributed to the Bi-*p* orbital and partly to the Rb-*p* and Na/K-*s* orbitals of these compounds. The conduction band of Na_2RbBi (K_2RbBi) is composed mainly of the Bi-*s*/*p*, Rb-*d* and Na-*s* (Bi-*s*/*p*, K-*d*, and Rb-*s*) orbitals.

TB-mBJ approach, these compounds are predicted to be semiconductors with direct bandgaps at the Gamma (G) point. The direct bandgaps of Na_2RbBi and K_2RbBi are 0.30 and 0.61 eV, respectively. To our best knowledge, no experimental or computational work has been done to determine the bandgap of these compounds. To understand the contribution of different orbitals to the electronic states and the hybridization distribution, we calculated the PDOSs and the total density of states (TDOSs) within the PBE-GGA approach, as shown in figure 3. The valence band in PDOS near the Fermi level is mainly attributable to the Bi-*p* orbital and partly from the Rb-*p* and Na/K-*s* orbitals of these compounds. The conduction band of Na_2RbBi (K_2RbBi) is composed mainly of the Bi-*s*/*p*, Rb-*d*, and Na-*s* (Bi-*s*/*p*, K-*d*, and Rb-*s*) orbitals. In the Na_2RbBi, there is a strong hybridization between Rb-*p* and Na-*s* states below the E_F, while above the E_F, there is a hybridization between Bi-*p* and Rb-*d*. There is a similar behavior in TB-mBJ approach, as shown in figure S6.

To investigate the TPT, we calculated the projected band structures of (Na, K)$_2$RbBi under different hydrostatic pressures within the PBE-GGA and TB-mBJ approaches, which are shown in figure 4. It can be seen that these compounds within GGA approach (see figures 4(a) and (c)) have no bandgap at ambient pressure ($V/V_0 = 1.0$). From the structure of the band provided in this case, it can be seen that the *s*–*p* band inversion does occur, i.e., the *p*-liked is above the *s*-liked bands. A hydrostatic lattice compression (HLC) ($V/V_0 = 0.88$ for Na_2RbBi and $V/V_0 = 0.80$ for K_2RbBi) is applied to determine the critical point of topological phase transition (CPTPT) (from nontrivial to trivial phase). This case is indicated by the black arrow in figure 4. To describe the CPTPT, the three-dimensional band structure and two-dimensional counter isolines of these compounds are shown in figure S7. As can be seen in this figure, the 3D band structure around the Dirac point consists of three band branches, the upper branch band of the Dirac cone (tagged with 1), the lower branch band of the Dirac cone (tagged with 3), and the band crossing through the Dirac point (tagged with 2). The energy isolines in the k_x–k_y plane indicate that the upper and lower branches band near the Dirac point are isotropic. Also, the band that crosses through the Dirac point is flat near the Fermi energy. As the HLC increases (e.g., $V/V_0 = 0.87$ for Na_2RbBi and $V/V_0 = 0.77$ for K_2RbBi) and passes this critical pressure, these compounds are transferred to the topologically trivial phase. In this case, the *s*-liked is above the *p*-liked bands, and a trivial bandgap is opened. Contrary to the GGA approach, these compounds within the TB-mBJ approach have a bandgap at ambient pressure. In this case, the order of the energy band is not reversed at the G point (the *s*-liked is above the *p*-liked bands). Therefore, by applying hydrostatic lattice tension (HLT), the TPT point can be achieved (see figures 4(b) and (d)). When V/V_0 is 1.11 for Na_2RbBi (1.22 for K_2RbBi), the trivial bandgap closes, and we reach the CPTPT (from trivial to nontrivial phase). At pressures above this critical pressure

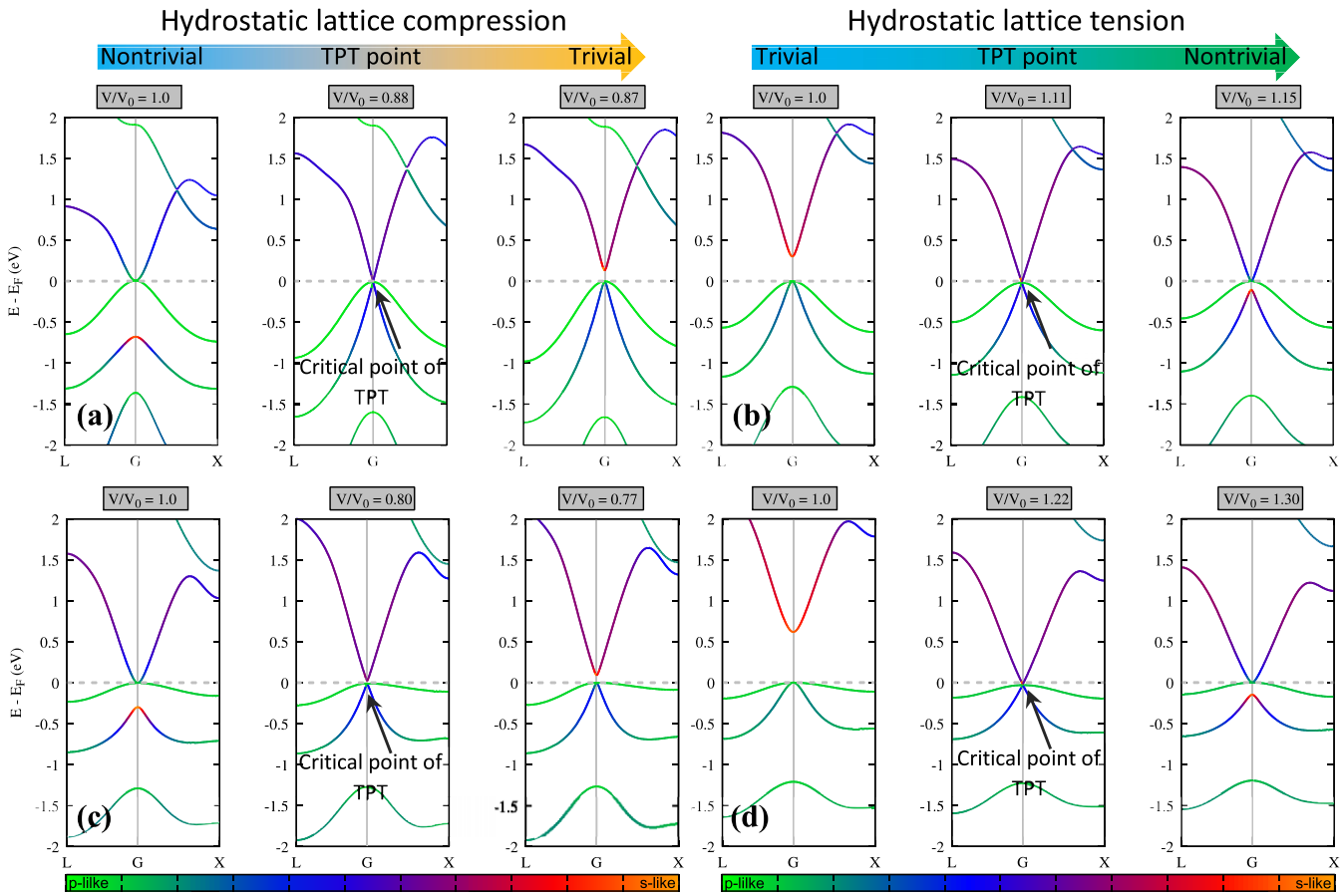

Figure 4. Projected band structures calculated with (a) and (c) PBE-GGA and (b) and (d) TB-mBJ functional including spin-orbit coupling for (a) and (b) Na_2RbBi and (c) and (d) K_2RbBi under HLC and HLT. These compounds within GGA approach have no band gap at ambient pressure ($V/V_0 = 1.0$). In this case, the s–p band inversion does occur; the p-liked is above the s-liked bands. Contrary to PBE-GGA approach, these compounds within TB-mBj approach have a bandgap at ambient pressure. In this case the order of the energy band is not reversed at the G point (the s-liked is above the p-liked bands). The CPTPT point is indicated by a black arrow. At pressures above the critical pressure, these compounds within mBJ (GGA) functional are transferred to the nontrivial (trivial) topological phase.

(e.g., $V/V_0 = 1.15$ for Na_2RbBi and $V/V_0 = 1.30$ for K_2RbBi), s–p band inversion occurs, and these compounds are transferred to the nontrivial topological phase. The mechanism is similar to the KNa_2Bi [46] and KNa_2Sb [47] compounds under hydrostatic pressure which also have the so-called s–p type band inversion. To better understand the topological nature, we study the atomic orbitals and consider the effect of HLC, HLT, and SOC on the energy levels at the G point for these compounds. This is schematically illustrated in figure 5. It should be noted that the energy levels near the Fermi level in this figure are mainly composed of Bi-6s and Bi-6p orbitals. Therefore, we focus on s and p orbitals of Bi and neglect the effect of other atomic orbitals. These orbitals are labeled as $s^{\pm}$ and $p^{\pm}$, where the superscript $(+, -)$ denotes the parity. In the PBE-GGA approach, before turning on the SOC, the s^+ orbital is above p^- orbital. When the SOC effect is taken into account in the equilibrium state ($V/V_0 = 1$), the degeneracy of the p^- level is lifted and split, and $p^-_{\pm 3/2}$ state is located above s^+ state. It is clear that in this case, the parity exchange. This introduces a nontrivial phase with inverted order of s^+ and $p^-_{\pm 3/2}$ (i.e., s–p band inversion). Therefore, the SOC effect has led to the TPT from the trivial to the nontrivial phase (see blue rectangle). By applying HLT at a volume rate $V/V_0 = \varepsilon_{HLC\_1}$, as an external effect, the CPTPT can be achieved (see purple rectangle). As the HLT increases (or the volumetric rate increases by $V/V_0 = \varepsilon_{HLC\_2}$), another TPT from the nontrivial phase to the trivial phase occurs (see blue rectangle). In this case, s^+ state is above $p^-_{\pm 3/2}$ state, and a nontrivial band gap is created. In the TB-mBJ approach, there is a similar mechanism, and only one TPT from the trivial phase to the nontrivial phase occurs due to HLC (see blue rectangle).

To confirm the topological phase before (after) the TPT point within the GGA (mBJ) approach, we calculated TSS and Z_2 topological index. $Z_2 = 1(0)$ indicates topological nontrivial (trivial) phase. The calculated projected surface DOSs at (001) surface (see figure 1(b)) and Wilson-loops around the WCCs along k_y are displayed in figure 6. Z_2 topological index can be determined using the number of crossings between any arbitrary horizontal reference line (green line) and the evolution of the WCCs. As shown in figures 6(a) and (b), the WCC lines cross the reference line an old (even) number of times for $k_x = 0$ and $k_x = 2\pi$ plane, respectively. Therefore, this result shows that $Z_2 = 1$. The calculated TSS at the semi-infinite (001) surface of these compounds are shown in figures 6(c)

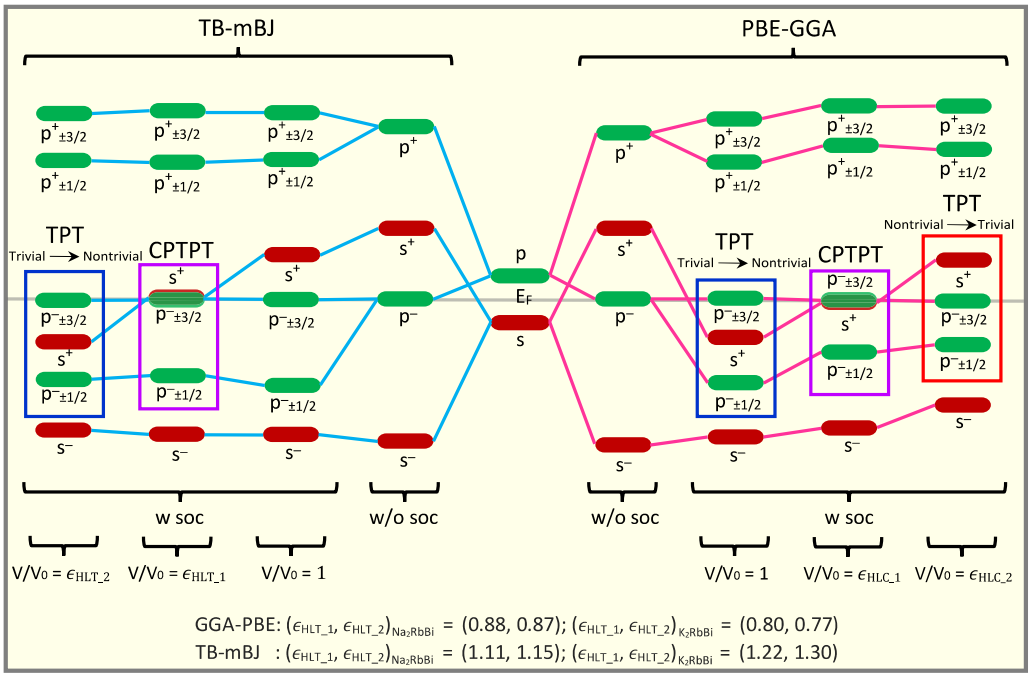

Figure 5. Schematic diagram of the evolution from the atomic *s* and *p* orbitals of Bi into the conduction and valence bands at the Gamma (G) point for (Na, K)$_2$RbBi compounds in the PBE-GGA and TB-mBJ approaches. The blue (red) and purple rectangles represent the TPT from trivial to nontrivial phase (from nontrivial to trivial phase) and the CPTPT, respectively.

and (d) (due to the similarity of the results, only the TSS within the PBE-GGA approach are shown in the figure). Since the band inversion occurs below the Fermi energy, the TSS appears below the E_F. Moreover, the TSS with a Dirac-type crossing is inside the projected valence bands due to the mixing of bulk electronic states. The black arrow shows the Dirac point.

3.3. Electrical transport properties and figure of merit

Boltzmann transport equation applied in BoltzTraP uses constant relaxation time approximation that can result in inaccurate transport coefficients. In order to accurately determine the TE properties, we calculate the carrier relaxation time using the DP theory described in section 2. The relaxation time is calculated by substituting E_i, C_i, m^*_{dos} in equation (1) (see section 2). The results of E_i, C_i, m^*_{dos}, and τ at 300 K for (Na, K)$_2$RbBi compounds within the PBE-GGA and TB-mBJ approaches at 300 K are listed in table 1. The results show that τ of the p-type Na$_2$RbBi/K$_2$RbBi within the TB-mBJ approach is larger than the corresponding value of the n-type one. In addition, the maximum τ of 792 fs is attributed to the p-type Na$_2$RbBi compound. The detailed results of relaxation time in both approaches are illustrated in figure S2.

The lattice thermal conductivity κ_l and the electronic thermal conductivity κ_e can be calculated separately. The κ_e can be obtained independently using the relaxation time. Furthermore, κ_l is calculated based on the modified Debye–Callaway model. The detailed results of $\kappa_{tot}(=\kappa_e + \kappa_l)$, κ_l, and κ_e as a function of the absolute temperature are shown in figure S8. It is noteworthy that the TE parameters considering TB-mBJ functional as the PBE-GGA functional underestimate the bandgap. However, all TE parameters within PBE-GGA are attached in the supporting information file.

The thermopower (or Seebeck coefficient) S, electrical conductivity, and PF of both the p-type and n-type (Na, K)$_2$RbBi compounds as a function of carrier concentration (n) at different temperatures, 300–900 K, are shown in figure 7. Due to the similarity in the electronic structure and band dispersion of the two compounds, a similar trend is observed in the thermopower of both compounds (see figures 7(a) and (b)). The slightly larger thermopower of K$_2$RbBi can be attributed to its larger bandgap. In these compounds, due to the high band degeneracy and large DOS, the thermopower of p-type is much larger than that of n-type. In the Na$_2$RbBi (K$_2$RbBi) compound, a high p-type thermopower (>450 μV K^{-1}) is obtained at 400 K (300 K) with a low doping concentration. The nonlinear behavior of the thermopower arises from the bipolar conduction effect resulting from the thermal excitation of minority carriers [73]. From figures 7(c) and (d), the maximum electrical conductivity for Na$_2$RbBi (K$_2$RbBi) is $\sim 5.9 \times 10^7$ 1/Ωm ($\sim 0.35 \times 10^7$ 1/Ωm) in the p-type region at room temperature. When the carrier concentration changes, the electrical conductivity and the absolute value of the thermopower of the compounds show opposite trends, as shown in figures 7(a)–(d). Therefore, the PF has a peak at an optimum carrier concentration. This peak, as shown, happens at a carrier concentration where both the thermopower and the electrical conductivity do not reach their maximum. Hence, the maximum n-type PF decreases for both compounds, while the maximum p-type PF increases with increasing temperature. The maximum PF of Na$_2$RbBi for p-type (n-type) doping at room temperature is about 36 (100) μW m^{-2} K^{-2}, nearly two (40) times that of K$_2$RbBi. The TE performance is directly related to electronic

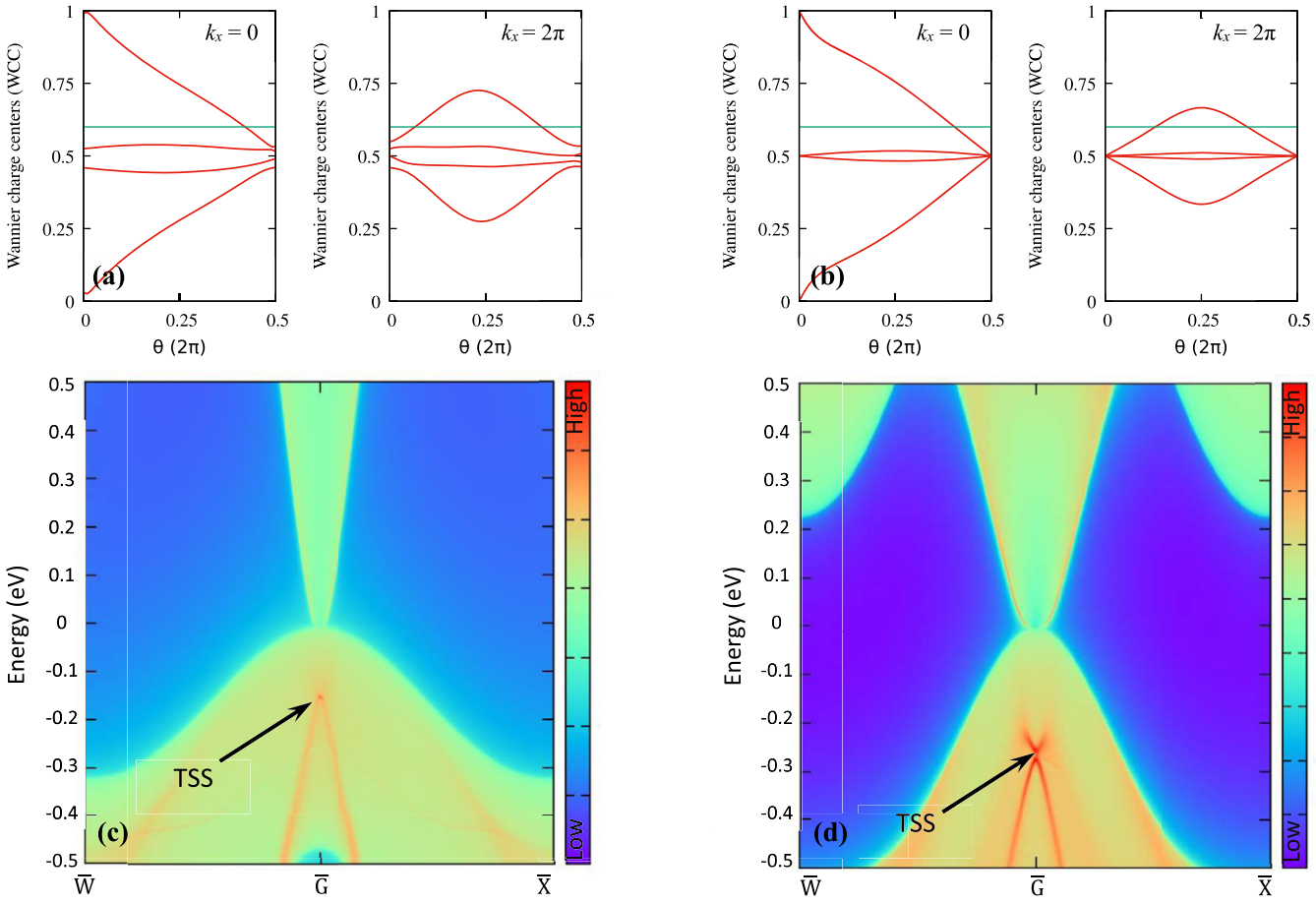

Figure 6. Evolution of the WCCs along k_y at $k_x = 0$ and $k_x = 2\pi$ planes for (a) Na_2RbBi and (b) K_2RbBi. The arbitrary reference line (green line) is shown for k_x planes. The calculated TSS for the semi-infinite (001) surface of (c) Na_2RbBi and (d) K_2RbBi. The TSS with a Dirac-type crossing is inside the projected valence bands due to the mixing with bulk electronic states. The black arrow shows the Dirac point.

Table 1. Elastic constant C_i (eV Å^{-3}), the DP constant E_i (eV), the DOSs effective mass m^*_{dos}, and the relaxation time τ (fs) of the (Na, K)$_2$RbBi compounds with PBE-GGA and TB-mBJ functionals at 300 K.

Compound	PBE-GGA							TB-mBJ						
		Hole			Electron			Hole				Electron		
	C_i	E_i	m^*_{dos}	τ	E_i	m^*_{dos}	τ	C_i	E_i	m^*_{dos}	τ	E_i	m^*_{dos}	τ
Na_2RbBi	0.22	6.73	0.22	270	6.73	0.41	100	0.22	10.5	0.06	792	6.29	0.12	775
K_2RbBi	0.77	5.93	0.12	305	5.93	0.17	175	0.77	9.5	0.13	98	5.42	0.36	66

transport [74–77]. So, to investigate the effect of this property, the total DOS as a function of carrier concentration at different temperatures of these compounds are calculated and displayed in figure S9. The results indicate that the total DOS in the p-type (total DOS of conduction bands) is more than that of the total DOS n-type (total DOS of valence bands) of these compounds. This result can lead to a larger Seebeck coefficient, and consequently, larger PF of the compounds in p-type than in n-type, as shown in figures 7(e) and (f). To calculate the total thermal conductivity, we have multiplied electronic thermal conductivity by τ and added it with lattice thermal conductivity. The results are shown in figures S2 and S8 as a function of absolute temperature. For the Na_2RbBi (K_2RbBi), κ_l is about 0.61 (1.17) W m^{-1} K^{-1} at 300 K. It decreases to about 0.17 (0.33) W m^{-1} K^{-1} with temperature increasing up to 1000 K. The Na_2RbBi and K_2RbBi compounds are expected to exhibit high TE performance. Such high TE performance arises primarily from a decent PF but ultralow lattice thermal conductivity near room temperature (high temperatures) in Na_2RbBi (K_2RbBi) compound. Figures 8(a) and (b) shows the total thermal conductivity (κ_{tot}) of these compounds, scaled by the relaxation time as a function of carrier concentration at different temperatures. It can be seen that, due to the ultralow lattice thermal conductivity, the electronic thermal conductivity significantly affects the total thermal conductivity. In both compounds, the electronic contribution to

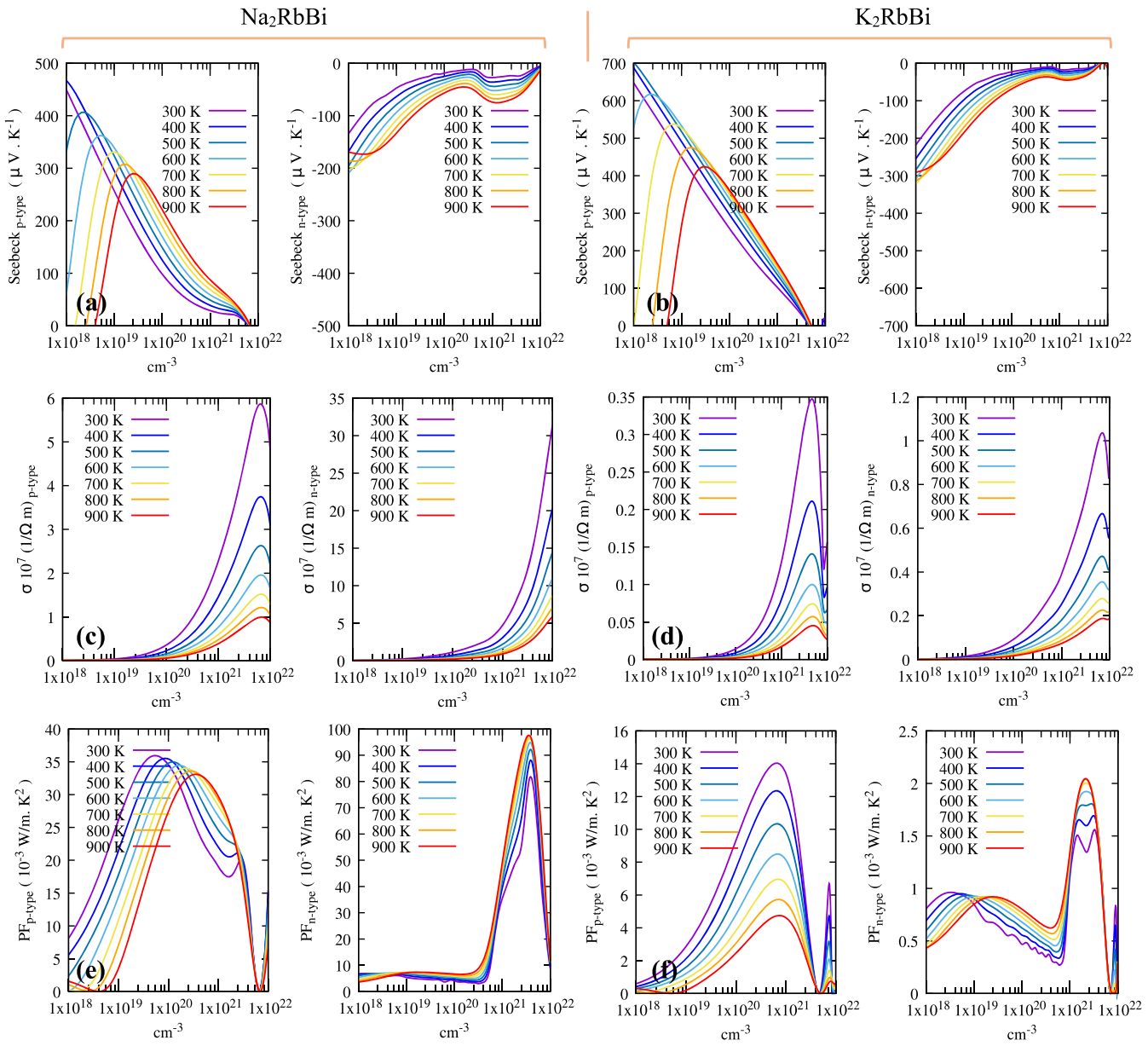

Figure 7. The calculated (a) and (b) Seebeck coefficient, (c) and (d) electrical conductivity, and (e) and (f) PF of p-type and n-type Na_2RbBi (left side of the page) and K_2RbBi (right side of the page) as a function of carrier concentration at different temperatures. The nonlinearity behavior of Seebeck coefficient arises from the bipolar conduction effect resulting from the thermal excitation of minority carriers. The absolute value of the thermopower and the electrical conductivity of these compounds follow opposite trends when the carrier concentration changes. Therefore, such behavior leads to a maximum PF at an optimum carrier concentration. For both compounds the maximum PF of n-type decreases, while the maximum PF of p-type increases with increasing the temperature.

heat conduction shows similar trends as electrical conductivity. Moreover, like electrical conductivity, the electronic part of the thermal conductivity for the n-type carrier in Na_2RbBi is also much higher than that of K_2RbBi and other carriers. Using the above-calculated transport coefficients, we estimate the zT of these compounds. Figures 8(c) and (d) shows zT as a function of temperature and carrier concentration. The lower κ_{tot}, 11.81 W m^{-1} K^{-1}, and high PF of Na_2RbBi at room temperature result in high zT values under p-type doping. For K_2RbBi compound, the PF is low at room temperature. κ_{tot} (11.57 W m^{-1} K^{-1}) is almost similar to Na_2RbBi compound at room temperature. Hence, the zT of this compound is lower than Na_2RbBi. However, at high temperatures, the κ_{tot} further decreases, leading to a high zT. A maximum zT of ∼0.80 (0.4) and ∼0.85 (0.52) were achieved under p-type (n-type) doping for Na_2RbBi and K_2RbBi at room and high temperature, respectively. For p-type doping, the 2D heat-maps of $zT(n, T)$ as a function of temperature (T) and carrier concentration (n) are shown in figures 8(e) and (f). While the zT of Na_2RbBi (K_2RbBi) is quite high over most of the region, a large $zT \sim 0.78$ (∼0.85) is obtained at the optimal condition, $n \sim 9.57 \times 10^{17}$ cm^{-3} and $T \sim 400$ K ($n \sim 4.39 \times 10^{20}$ cm^{-3} and $T = 1000$ K). Another interesting observation is that the zT of p-type (Na, K)$_2$RbBi is a weak function of temperature.

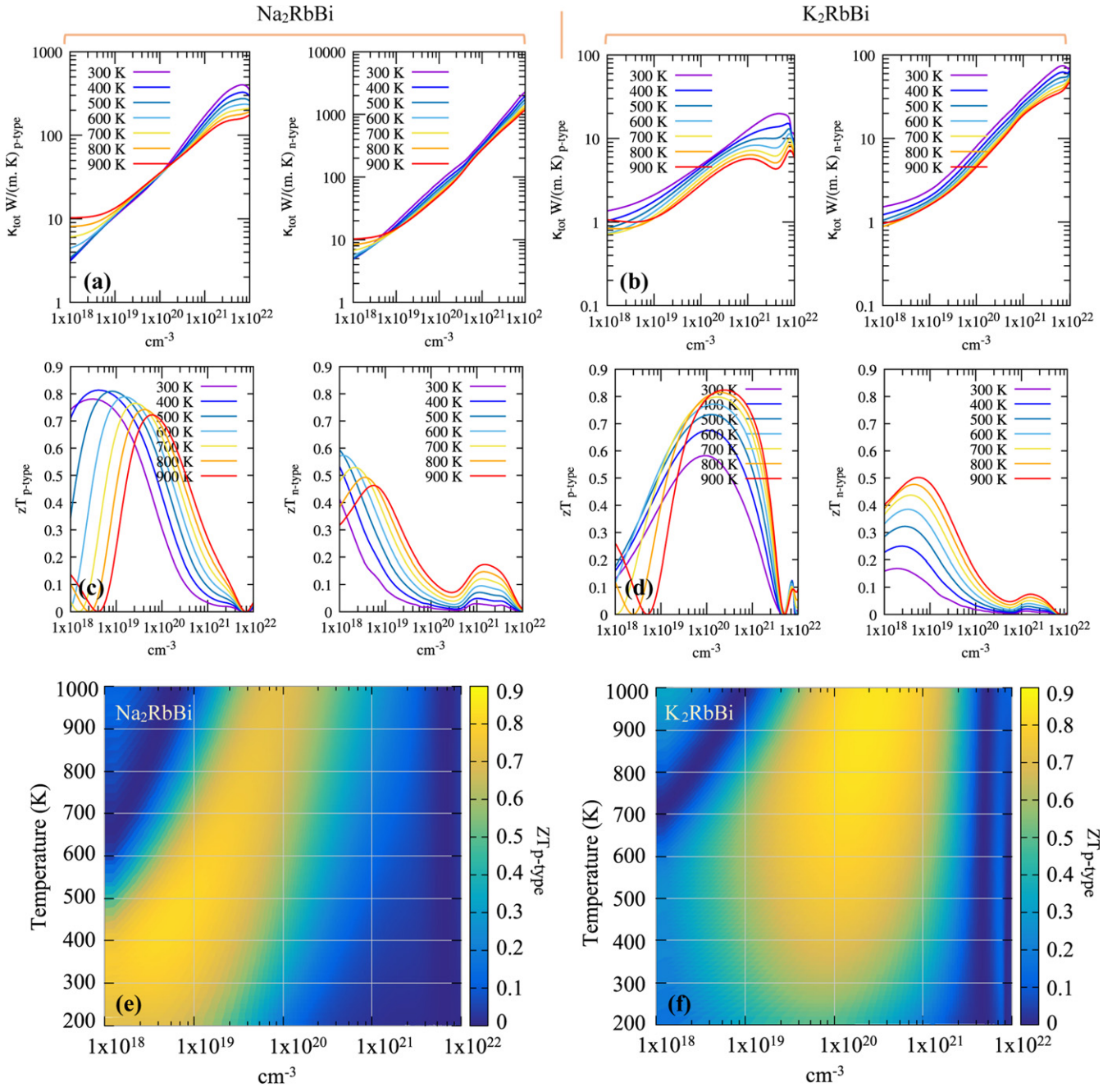

Figure 8. The calculated (a) and (b) total thermal conductivity (κ_{tot}), and (c) and (d) figure of merit zT of p-type and n-type Na_2RbBi (left side of the page) and K_2RbBi (right side of the page) as a function of carrier concentration at different temperatures. The 2D heat-maps of $zT(n, T)$ as a function of temperature (T) and carrier concentration (n) is plotted in (e) and (f). A maximum zT of ∼0.80 (0.4) and ∼0.85 (0.52) were achieved under p-type (n-type) doping for Na_2RbBi and K_2RbBi at room and high temperature, respectively. While the zT of Na_2RbBi (K_2RbBi) is quite high over most of the region, a large $zT \sim 0.78$ (∼0.85) is obtained at the optimal condition, $n \sim 9.57 \times 1017$ cm^{-3} and $T \sim 400$ K ($n \sim 4.39 \times 1020$ cm^{-3} and $T = 1000$ K).

For example, the zT of p-type Na_2RbBi (K_2RbBi) remains in the range of 0.52–0.73 (0.58–0.8) at a fixed doping concentration of 3.5×10^{19} cm^{-3} (1.22×10^{20} cm^{-3}) in the entire temperature range of 300–900 K. This is especially interesting as it expands over the temperature range of many energy harvesting applications.

4. Conclusion

We presented a transition from semiconductor trivial topological phase to semimetallic nontrivial topological phase via external hydrostatic pressure on (Na, $K)_2RbBi$ compounds based on first-principles calculations. The band inversion,

hence the TSS, occurs below the Fermi energy. Moreover, the TSS with a Dirac-type crossing is ∼280 meV inside the projected valence bands due to mixing bulk electronic states. The electronic and thermal transport properties of both compounds, including the lattice thermal conductivity, electronic thermal conductivity, and the charge carrier relaxation time, were further investigated using the first principles, the Boltzmann transport equation, and the DPT. The lattice dynamic calculations indicate strong anharmonic scattering between acoustic phonons in Na_2RbBi and K_2RbBi, leading to an exceptionally low lattice thermal conductivity at room temperature (∼0.6–1 W m^{-1} K^{-1}). Furthermore, the analyses of the elastic constants indicate that K_2RbBi has a NPR. Likewise, we find both compounds are dynamically and mechanically stable from elastic constants and phonon dispersion, indicating their synthesis feasibility. Therefore, these topological compounds offer good candidates for TE device applications operated over a broad temperature range.

Acknowledgments

Kavous Ataei is acknowledged for the valuable comments on relaxation time calculation. This study is partially supported by the National Science Foundation (NSF) under Grant Numbers ECCS-1711253 and CBET-2110603.

Data availability statement

The data that support the findings of this study are available upon reasonable request from the authors.

ORCID iDs

Shahram Yalameha https://orcid.org/0000-0002-9873-5659
Daryoosh Vashaee https://orcid.org/0000-0003-3667-3672

References

[1] Narimani M, Yalameha S and Nourbakhsh Z 2020 High thermoelectric efficiency of La*X* (*X* = Sb, Bi) two dimensional topological insulators *J. Phys.: Condens. Matter.* **32** 255501
[2] Wang Q, Hu Z and Shao X 2020 Exploring electronic, optoelectronic, and thermoelectric properties of ternary compound $MgSrSe_2$ from first-principles study *AIP Adv.* **10** 045010
[3] Müchler L, Casper F, Yan B, Chadov S and Felser C 2013 Topological insulators and thermoelectric materials *Phys. Status Solidi* **7** 91–100
[4] Pei Y, Wang H and Snyder G J 2012 Band engineering of thermoelectric materials *Adv. Mater.* **24** 6125–35
[5] Norouzzadeh P and Vashaee D 2016 Classification of valleytronics in thermoelectricity *Sci. Rep.* **6** 1–15
[6] Norouzzadeh P, Myles C W and Vashaee D 2013 Prediction of a large number of electron pockets near the band edges in type-VIII clathrate Si-46 and its physical properties from first principles *J. Phys.: Condens. Matter.* **25** 475502
[7] Snyder G J and Toberer E S 2011 Complex thermoelectric materials *Materials for Sustainable Energy: A Collection of Peer-Reviewed Research and Review Articles from Nature Publishing Group* (London: Nature Publishing Group) pp 101–10
[8] Norouzzadeh P, Myles C W and Vashaee D 2014 Prediction of giant thermoelectric power factor in type-VIII clathrate Si 46 *Sci. Rep.* **4** 1–5
[9] Gayner C and Amouyal Y 2020 Energy filtering of charge carriers: current trends, challenges, and prospects for thermoelectric materials *Adv. Funct. Mater.* **30** 1901789
[10] Vashaee D and Shakouri A 2004 Nonequilibrium electrons and phonons in thin film thermionic coolers *Microscale Thermophys. Eng.* **8** 91–100
[11] Heremans J P, Jovovic V, Toberer E S, Saramat A, Kurosaki K, Charoenphakdee A, Yamanaka S and Snyder G J 2008 Enhancement of thermoelectric efficiency in PbTe by distortion of the electronic density of states *Science* **321** 554–7
[12] Vashaee D, Zhang Y, Shakouri A, Zeng G and Chiu Y-J 2006 Cross-plane Seebeck coefficient in superlattice structures in the miniband conduction regime *Phys. Rev.* B **74** 195315
[13] Vashaee D and Shakouri A 2006 HgCdTe superlattices for solid-state cryogenic refrigeration *Appl. Phys. Lett.* **88** 132110
[14] Sumithra S, Takas N J, Misra D K, Nolting W M, Poudeu P F P and Stokes K L 2011 Enhancement in thermoelectric figure of merit in nanostructured Bi_2Te_3 with semimetal nanoinclusions *Adv. Energy Mater.* **1** 1141–7
[15] Satyala N, Tahmasbi Rad A, Zamanipour Z, Norouzzadeh P, Krasinski J S, Tayebi L and Vashaee D 2014 Reduction of thermal conductivity of bulk nanostructured bismuth telluride composites embedded with silicon nano-inclusions *J. Appl. Phys.* **115** 044304
[16] Satyala N, Krasinski J S and Vashaee D 2014 Simultaneous enhancement of mechanical and thermoelectric properties of polycrystalline magnesium silicide with conductive glass inclusion *Acta Mater.* **74** 141–50
[17] Novak T G, Kim K and Jeon S 2019 2D and 3D nanostructuring strategies for thermoelectric materials *Nanoscale* **11** 19684–99
[18] Zamanipour Z, Shi X, Dehkordi A M, Krasinski J S and Vashaee D 2012 The effect of synthesis parameters on transport properties of nanostructured bulk thermoelectric p-type silicon germanium alloy *Phys. Status Solidi a* **209** 2049–58
[19] Uher C 2001 Skutterudites: prospective novel thermoelectrics *Semiconductors and Semimetals* (Amsterdam: Elsevier) pp 139–253
[20] Dresselhaus M *et al* 2007 Nanocomposites to enhance *ZT* in thermoelectrics *MRS Online Proc. Library Archive* vol 1044
[21] Satyala N, Norouzzadeh P and Vashaee D 2014 Nano bulk thermoelectrics: concepts, techniques, and modeling *Nanoscale Thermoelectrics* (Berlin: Springer) pp 141–83
[22] Thesberg M, Pourfath M, Kosina H and Neophytou N 2015 The influence of non-idealities on the thermoelectric power factor of nanostructured superlattices *J. Appl. Phys.* **118** 224301
[23] Pichanusakorn P and Bandaru P 2010 Nanostructured thermoelectrics *Mater. Sci. Eng. R: Rep.* **67** 19–63
[24] Satyala N and Vashaee D 2012 Detrimental influence of nanostructuring on the thermoelectric properties of magnesium silicide *J. Appl. Phys.* **112** 093716
[25] Norouzzadeh P, Zamanipour Z, Krasinski J S and Vashaee D 2012 The effect of nanostructuring on thermoelectric transport properties of p-type higher manganese silicide MnSi1.73 *J. Appl. Phys.* **112** 124308
[26] Zamanipour Z, Krasinski J S and Vashaee D 2013 Comparison of boron precipitation in p-type bulk nanostructured and polycrystalline silicon germanium alloy *J. Appl. Phys.* **113** 143715

[27] Polash M M H, Yalameha S, Zhou H, Ahadi K, Nourbakhsh Z and Vashaee D 2021 Topological quantum matter to topological phase conversion: fundamentals, materials, physical systems for phase conversions, and device applications *Mater. Sci. Eng. R: Rep.* **145** 100620

[28] Ning S, Huang S, Zhang Z, Zhang R, Qi N and Chen Z 2020 High thermoelectric performance of topological half-Heusler compound LaPtBi achieved by hydrostatic pressure *Phys. Chem. Chem. Phys.* **22** 14621–9

[29] Hor Y S, Richardella A, Roushan P, Xia Y, Checkelsky J G, Yazdani A, Hasan M Z, Ong N P and Cava R J 2009 p-type Bi_2Se_3 for topological insulator and low-temperature thermoelectric applications *Phys. Rev.* B **79** 195208

[30] Takahashi R and Murakami S 2012 Thermoelectric transport in topological insulators *Semicond. Sci. Technol.* **27** 124005

[31] Xu N, Xu Y and Zhu J 2017 Topological insulators for thermoelectrics *npj Quantum Mater.* **2** 1–9

[32] Fu C, Sun Y and Felser C 2020 Topological thermoelectrics *APL Mater.* **8** 040913

[33] Yan B and Felser C 2017 Topological materials: Weyl semimetals *Annu. Rev. Condens. Matter Phys.* **8** 337–54

[34] Xiang J, Hu S, Lyu M, Zhu W, Ma C, Chen Z, Steglich F, Chen G and Sun P 2020 Large transverse thermoelectric figure of merit in a topological Dirac semimetal *Sci. China Phys. Mech. Astron.* **63** 1–7

[35] Fu C *et al* 2018 Large Nernst power factor over a broad temperature range in polycrystalline Weyl semimetal NbP *Energy Environ. Sci.* **11** 2813–20

[36] Wang H *et al* 2018 Magnetic-field enhanced high-thermoelectric performance in topological Dirac semimetal Cd_3As_2 crystal *Sci. Bull.* **63** 411–8

[37] Skinner B and Fu L 2018 Large, nonsaturating thermopower in a quantizing magnetic field *Sci. Adv.* **4** eaat2621

[38] Liang T, Lin J, Gibson Q, Gao T, Hirschberger M, Liu M, Cava R J and Ong N P 2017 Anomalous Nernst effect in the Dirac semimetal Cd_3As_2 *Phys. Rev. Lett.* **118** 136601

[39] Kalarasse L, Bennecer B and Kalarasse F 2010 Optical properties of the alkali antimonide semiconductors Cs_3Sb, Cs_2KSb, CsK_2Sb and K_3Sb *J. Phys. Chem. Solids* **71** 314–22

[40] Amador R and Cocchi C 2021 Electronic structure and optical properties of Na_2KSb and NaK_2Sb from first-principles many-body theory (arXiv:2104.08513)

[41] Kalarasse L, Bennecer B and Kalarasse F 2011 Elastic and electronic properties of the alkali pnictide compounds Li_3Sb, Li_3Bi, Li_2NaSb and Li_2NaBi *Comput. Mater. Sci.* **50** 2880–5

[42] Spicer W E 1958 Photoemissive, photoconductive, and optical absorption studies of alkali-antimony compounds *Phys. Rev.* **112** 114

[43] Sommer A H 1955 New photoemissive cathodes of high sensitivity *Rev. Sci. Instrum.* **26** 725–6

[44] Rusinov I P, Sklyadneva I Y, Heid R, Bohnen K-P, Petrov E K, Koroteev Y M, Echenique P M and Chulkov E V 2017 Nontrivial topology of cubic alkali bismuthides *Phys. Rev.* B **95** 224305

[45] Nie T, Meng L, Li Y, Luan Y and Yu J 2018 Phase transition studies of Na_3Bi system under uniaxial strain *J. Phys.: Condens. Matter.* **30** 125502

[46] Sklyadneva I Y, Rusinov I P, Heid R, Bohnen K-P, Echenique P M and Chulkov E V 2016 Pressure-induced topological phases of KNa_2Bi *Sci. Rep.* **6** 1–9

[47] Yalameha S, Nourbakhsh Z and Vaez A 2018 Hydrostatic strain-induced topological phase of KNa_2Sb *J. Magn. Magn. Mater.* **468** 279–86

[48] Blaha P, Schwarz K, Sorantin P and Trickey S B 1990 Full-potential, linearized augmented plane wave programs for crystalline systems *Comput. Phys. Commun.* **59** 399–415

[49] Blaha P, Schwarz K, Tran F, Laskowski R, Madsen G K H and Marks L D 2020 WIEN2k: an APW+lo program for calculating the properties of solids *J. Chem. Phys.* **152** 074101

[50] Perdew J P, Burke K and Ernzerhof M 1996 Generalized gradient approximation made simple *Phys. Rev. Lett.* **77** 3865

[51] Tran F and Blaha P 2009 Accurate band gaps of semiconductors and insulators with a semilocal exchange–correlation potential *Phys. Rev. Lett.* **102** 226401

[52] Togo A and Tanaka I 2015 First principles phonon calculations in materials science *Scr. Mater.* **108** 1–5

[53] Madsen G K H and Singh D J 2006 BoltzTraP. A code for calculating band-structure dependent quantities *Comput. Phys. Commun.* **175** 67–71

[54] Fan T and Oganov A R 2020 AICON: a program for calculating thermal conductivity quickly and accurately *Comput. Phys. Commun.* **251** 107074

[55] Jamal M *et al* 2014 IRelast package *Journal of Alloys and Compounds* **735** 569–79

[56] Yalameha S, Nourbakhsh Z and Vashaee D 2021 ElATools: a tool for the analysis of anisotropic elastic properties in the 2D and 3D materials (arXiv:2105.07279)

[57] Xue Q Y, Liu H J, Fan D D, Cheng L, Zhao B Y and Shi J 2016 LaPtSb: a half-Heusler compound with high thermoelectric performance *Phys. Chem. Chem. Phys.* **18** 17912–6

[58] Bardeen J and Shockley W 1950 Deformation potentials and mobilities in non-polar crystals *Phys. Rev.* **80** 72

[59] Rubel O, Tran F, Rocquefelte X and Blaha P 2021 Perturbation approach to *ab initio* effective mass calculations *Comput. Phys. Commun.* **261** 107648

[60] Sun H-L, Yang C-L, Wang M-S and Ma X-G 2020 Remarkably high thermoelectric efficiencies of the half-Heusler compounds B*X*Ga (X = Be, Mg, and Ca) *ACS Appl. Mater. Interfaces* **12** 5838–46

[61] Pizzi G *et al* 2020 Wannier90 as a community code: new features and applications *J. Phys.: Condens. Matter.* **32** 165902

[62] Sancho M P L, Sancho J M L, Sancho J M L and Rubio J 1985 Highly convergent schemes for the calculation of bulk and surface Green functions *J. Phys. F: Met. Phys.* **15** 851

[63] Gresch D, Autes G, Yazyev O V, Troyer M, Vanderbilt D, Bernevig B A and Soluyanov A A 2017 Z2Pack: numerical implementation of hybrid Wannier centers for identifying topological materials *Phys. Rev.* B **95** 075146

[64] Batra N and Sheet G 2020 Physics with coffee and doughnuts: understanding the physics behind topological insulators through Su–Schrieffer–Heeger model *Resonance* **25** 765–86

[65] Yu R, Qi X L, Bernevig A, Fang Z and Dai X 2011 Equivalent expression of Z_2 topological invariant for band insulators using the non-Abelian Berry connection *Phys. Rev.* B **84** 075119

[66] Mukherjee A, Nandy A, Sil S and Chakrabarti A 2020 Engineering topological phase transition and Aharonov–Bohm caging in a flux-staggered lattice *J. Phys.: Condens. Matter.* **33** 035502

[67] Dias R G and Marques A M 2021 Matryoshka approach to sine–cosine topological models *Phys. Rev.* B **103** 245112

[68] Soluyanov A A and Vanderbilt D 2011 Computing topological invariants without inversion symmetry *Phys. Rev.* B **83** 235401

[69] Marques A M, Madail L and Dias R G 2021 One-dimensional 2n-root topological insulators and superconductors *Phys. Rev.* B **103** 235425

[70] Wallace D C and Callen H 1972 Thermodynamics of crystals *Am. J. Phys.* **40** 1718–9

[71] Chan M K Y and Ceder G 2010 Efficient band gap prediction for solids *Phys. Rev. Lett.* **105** 196403
[72] Sharma S, Singh B and Kumar P 2018 A comparative study of thermoelectric properties of $CuGaTe_2$ by using PBE and MBJ potentials *AIP Conf. Proc.* **1942** 140036
[73] Gong J J, Hong A J, Shuai J, Li L, Yan Z B, Ren Z F and Liu J-M 2016 Investigation of the bipolar effect in the thermoelectric material $CaMg_2Bi_2$ using a first-principles study *Phys. Chem. Chem. Phys.* **18** 16566–74
[74] Mukherjee A and Nandy A 2019 Spectral engineering and tunable thermoelectric behavior in a quasiperiodic ladder network *Phys. Lett.* A **383** 570–7
[75] Maciá E 2010 Codon thermoelectric signature in molecular junctions *Phys. Rev.* B **82** 045431
[76] Maciá E 2007 DNA-based thermoelectric devices: a theoretical prospective *Phys. Rev.* B **75** 035130
[77] Datta S 2005 *Quantum Transport: Atom to Transistor* (Cambridge: Cambridge University Press)